TNO innovation for life

TNO WP4 activities

Blade Extensions for Silent Turbines (BEST): Numerical toolbox development

TNO Public › TNO 2025 R13194
December 2025

Energy & Materials Transition
www.tno.nl
+31 88 866 50 65
info@tno.nl

TNO 2025 R13194 – December 2025

Blade Extensions for Silent Turbines (BEST): Numerical toolbox development

TNO WP4 activities

Author(s)	M. Caboni, A. Koodly Ravishankara, K. Boorsma

Classification report	TNO Public
Number of pages	34 (excl. front and back cover)
Number of appendices	0
Sponsor	RvO
Project name	Blade Extensions for Silent Turbines (BEST)
Project number	060.54912

Summary

This document summarizes the activities performed by TNO within “WP4: Numerical toolbox development” of the Blade Extensions for Silent Turbines (BEST) project. In this work package, TNO developed and applied numerical models to simulate the noise reduction achieved by the permeable trailing edge add-ons, named MuteSkin, developed by MuTech. Specifically, TNO investigated this technology using a computational fluid dynamics (CFD) model based on the Reynolds-Averaged Navier-Stokes (RANS) equations and the engineering model developed by Brooks, Pope, and Marcolini (BPM). The CFD model was employed to examine the impact of the MuteSkin add-on on the aerodynamic conditions of the blades compared to blades without add-ons. The BPM model, originally designed for nominal blades without trailing edge add-ons, was modified to include the effect of MuteSkin on blade noise. The modification aimed at fine-tuning specific BPM model parameters using wind tunnel data. CFD simulations have shown that the boundary layer remains largely unaffected by the presence of MuteSkin-like add-ons. Moreover, it was found that the RANS approach fails to adequately capture the mechanisms responsible for noise reduction. Conversely, the modified BPM model, using the chosen tuning parameters, successfully replicated the experimental noise spectra for profiles equipped with MuTech’s add-ons.

BEST has been co-financed with Topsector Energiesubsidie from the Dutch Ministry of Economic Affairs under grant number HER+22-02-03415120.

Contents

1 Introduction

The Blade Extensions for Silent Turbines (BEST) project aimed to develop and prepare for industrial implementation a trailing edge noise mitigation add-on for wind turbine blades, using a permeable material called MuteSkin, developed by a TU Delft spin-off company named MuTech. The BEST project included various work packages (WPs) focusing on wind tunnel and field acoustic measurements, material development, manufacturing, and more. TNO participated in a WP, focused on developing numerical methods, named "WP4: Numerical toolbox development". Within this WP, TNO faced the challenge of developing and using numerical methodologies to compute the effect of MuTech's add-ons on the noise production of wind turbine blades. Most of the existing and industrially used methodologies are in fact primarily developed for blades without trailing edge add-ons. This report summarizes the main activities and findings of TNO within this WP.

TNO focused on two main numerical methodologies: one based on the Reynolds-Averaged Navier-Stokes (RANS) equations and the other on the engineering model developed by Brooks, Pope, and Marcolini (BPM). The RANS model was used to explore the average aerodynamic conditions of an airfoil with and without the trailing-edge add-ons. The widely used BPM model was modified to incorporate the effects of generic trailing edge noise mitigation add-ons for wind turbine blades, for which wind tunnel data is available. The methodology involves fine-tuning certain BPM parameters to align the model output with wind tunnel data. Details on the modifications to the BPM model to include trailing edge noise mitigation add-ons for wind turbine blades, as conducted by TNO in this project, were published in [1]. Significant parts of this publication are included in this report. Both the RANS analysis and the modifications to the BPM model were derived from 2D airfoil simulations and measurements.

This report is organized in three technical chapters. Chapter 2 discusses the RANS simulations conducted on porous materials. Chapter 3 validates the BPM model for turbulent boundary layer trailing edge noise using the BANC database [2, 3, 4, 5], and databases on the NACA-0018 and FFA-W3-211 profile. The latter two databases, provided by MuTech, are based on measurements taken in the A-tunnel at TU Delft (March 2024) and in the Poul la Cour Tunnel at DTU (December 2024). Chapter 4 details the modification of the BPM model for trailing edge noise mitigation add-ons, utilizing the A-tunnel NACA-0018 database, and applies the modified model to rotor simulations.

2 RANS modelling of porous media for aeroacoustic applications

2.1 Background

This section outlines the outcome of using the RANS approach in OpenFOAM to model the flow through porous media, to derive aerodynamic quantities for noise computations. Porous materials are commonly used to reduce aerodynamic noise. The flow around the NACA 0018 airfoil with a solid and porous trailing edge is simulated and the numerical results are compared against experimental measurements. The details are provided below.

2.2 Numerical modeling of porous materials

Flow through porous media is studied widely by researchers for oil recovery and groundwater modeling [6]. The porous medium is modeled as an equivalent fluid region that mimics the presence of the porous medium by a volume force that depends on material properties as described by Darcy's law [7]. OpenFOAM [8] is used to model the flow through porous media.

2.2.1 OpenFOAM implementation

The momentum equation of the Navier Stokes equation is modified as [9]

$$\frac{\partial \rho \mathsf{U}}{\partial t} + \nabla \left(\rho \mathsf{U}\mathsf{U}\right) = \nabla \sigma + S_m, \tag{2.1}$$

where U is the velocity vector, ρ is the density, σ is the total stress tensor including pressure and shear rate and S_m is the extra source term introduced to model the momentum loss due to the porous material.

$$S_m = \left(\mu \mathsf{D} + \frac{1}{2}\rho \cdot tr(\mathsf{U} \cdot \mathsf{IF})\right) \mathsf{U}. \tag{2.2}$$

The code snippet to specify the properties of the porous material is

Listing 2.1: Porous material set up in OpenFOAM

```
porosity1
{
   type DarcyForchheimer;

   cellzone porous;

   d (d1 d2 d3);
   f (f1 f2 f3);

   coordinateSystem
   {
```

```
        type cartesian;
        origin (0 0 0);
        coordinateRotation
        {
            type axesRotation;
            e1 (0 1 0);
            e2 (0 0 1);
        }
    }
}
```

D and F are model constants that are specified as inputs. Calculation of these constants according to Teruna et al [10] is

$$\mathsf{D} = \frac{\nu}{\mathsf{K}} \tag{2.3}$$

where K is the permeability of the porous material, ν is fluid kinematic viscosity and

$$\mathsf{F} = \mathsf{C} \tag{2.4}$$

where C is the form coefficient of the material. In OpenFOAM, the model constants must be specified as d and f along coordinate axes $e1$, $e2$, $e3$, to account for different porosity properties along different directions. Only the axes $e1$ and $e2$ have to be specified in the file and $e3$ is calculated to be perpendicular to both of them.

Reynolds number	D	F
2.7×10^5	1371.74	2613.0
5.4×10^5	685.8	2613.0

Table 2.1: D and F paramters for different Reynolds numbers.

2.3 Preliminary results

2.3.1 Validation set-up

Validation of the model is performed by comparing the numerical results against experimental data from Teruna at al [10, 11], which showed a significant noise reduction through application of a porous trailing edge on a NACA0018 profile. The operating conditions are listed in table 2.2. This case is chosen due to the availability of flow and acoustic data, despite the Reynolds number being considerably lower than those observed on modern wind turbines.

Parameters	Values
Reynolds number	2.7×10^5
Angle of attack (°)	$0°, 7.8°$
Incoming velocity	20 m/s

Table 2.2: Flow parameters for RANS simulation [10, 11].

2.3.2 Grid refinement

Grid refinement was performed at an angle of attack of $\alpha = 7.8°$. Three grids were considered by varying the number of points on the airfoil surface, with 128 (lvl1), 256 (lvl2) and 512 (lvl3) points. The residual of the x momentum and the lift coefficient for the three grids is shown in figure 2.1. The grid with 256 points on the surface of the airfoil was chosen for further analysis.

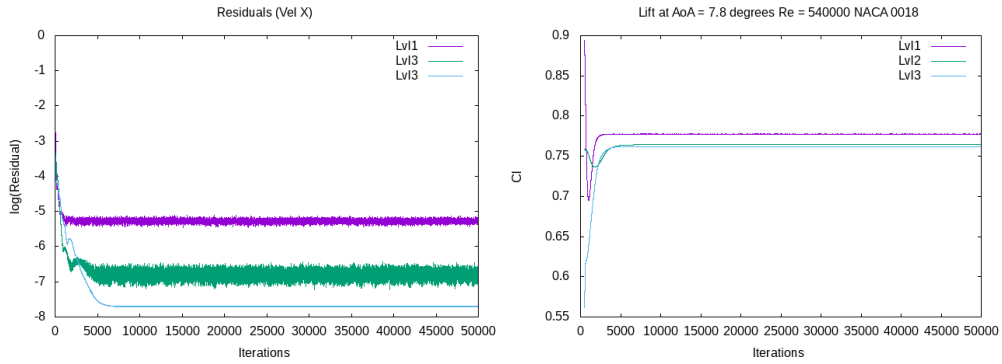

Figure 2.1: Residual and lift coefficient for the NACA 0018 case, featuring the lvl1, lvl2 and lvl3 grids.

2.3.3 Porous region definition

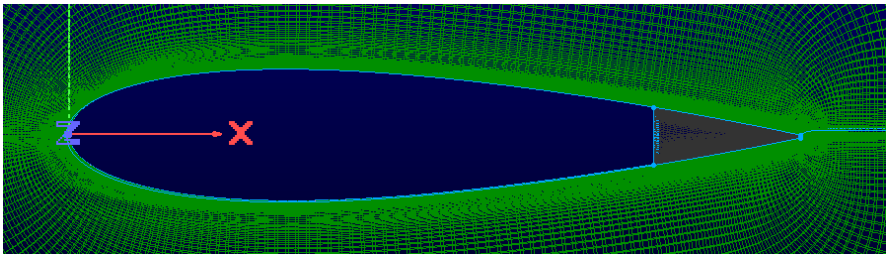

Figure 2.2: Airfoil mesh for porous TE. Grey part is the porous insert.

The gray region in figure 2.2 is considered to be porous. The porous parameters used are defined in table 2.1. An isotropic porous medium was assumed for the simulations.

2.3.4 Results

The velocity and pressure for the solid TE and the porous TE near the trailing edge at $x/c = 0.99$ are shown in figure 2.3. The velocity profiles from the two cases are very similar while a pressure loss is observed with porous TE. The resulting displacement thicknesses for the clean and porous simulations are respectively $\delta^*/c = 0.052$ and $\delta^*/c = 0.041$.

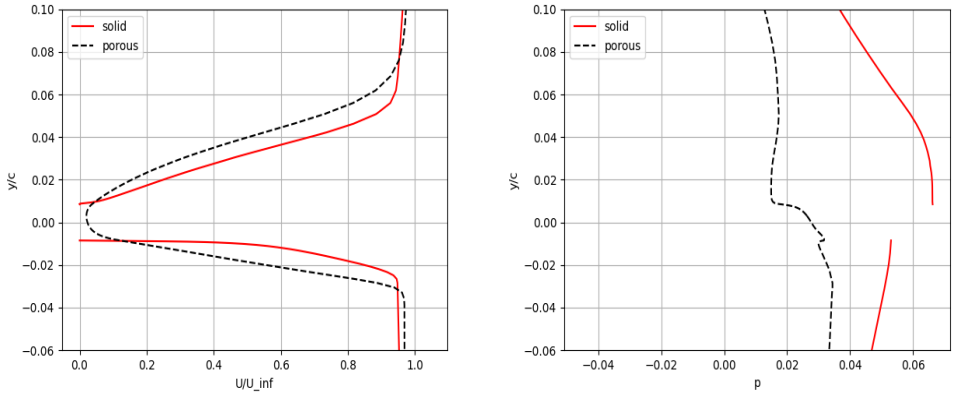

Figure 2.3: Numerical velocity and pressure profiles at $x/c = 0.99$ for solid and porous TE.

2.4 Conclusions

The resulting boundary layer is not significantly different to that of a clean airfoil as evidenced by the displacement thicknesses being very similar. Considering the BPM [12] and other engineering type noise prediction models make use of these time-averaged boundary layer parameters, these small differences are not sufficient to explain the noise reduction. Hence, in agreement with the work reported in [11], it is acknowledged that the mechanisms responsible for the noise reduction cannot be captured adequately by RANS simulations. Furthermore, considering that the design of porous extensions is confidential, simulation of the detailed flow is not possible. Hence no further efforts are undertaken to model the effect of porous trailing edges using CFD simulations.

3 Validation of Brooks, Pope, and Marcolini's model for turbulent boundary layer trailing edge noise

3.1 Background and theory

Brooks *et al.* [12] developed shape and amplitude functions to describe the 1/3-octave spectral characteristics of the TBL-TE noise mechanism. Mirroring the behavior of the measurements shown in the example in Figure 3.1, the modeled spectra display a concave down, parabola-like shape, defined by a peak frequency (or Strouhal number), shape, and level. Brooks *et al.* [12] empirically derived the spectral shape and amplitude functions from an extensive database of acoustic measurements conducted on various NACA-0012 airfoil blade sections with different chords, Mach and Reynolds numbers, and angles of attack.

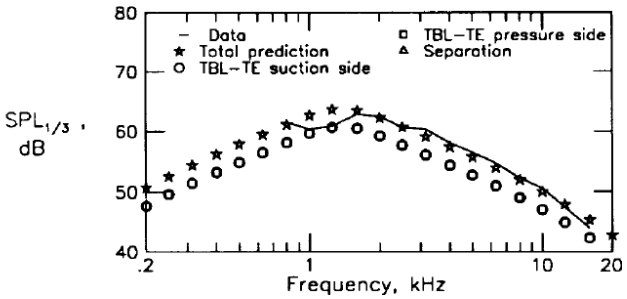

Figure 3.1: Example of comparison between measured and predicted spectra of turbulent boundary layer trailing-edge noise. Image reproduced from Brooks *et al.* [12].

The derivation of the BPM model for turbulent boundary layer trailing edge noise, as described by Brooks *et al.* [12], began with calculating a scaled sound pressure level for each experimental condition from the referenced database. This is done by subtracting a semi-empirical scaling function, which is based on the analysis by Ffowcs Williams and Hall *et al.* [13], from the total sound pressure level, as follows:

$$\text{Scaled SPL}_{(1/3)} = \text{SPL}_{(1/3)} - 10\log\left(\frac{\delta_s^* M^5 L}{r_e^2}\right) \tag{3.1}$$

As seen in Eq. (3.1), the scaling function is proportional to the fifth power of the Mach number (M), the trailing edge boundary layer displacement thickness on the suction side (δ_s^*)[1], and the span-wise length wetted by the flow (L), while being inversely proportional to the square of the observer distance (r_e). The relationship between the scaling function and the fifth power of

[1] In the following, the index s refers to the suction side, while the index p refers to the pressure side.

velocity has been confirmed in several studies Brooks *et al.* [12]. Brooks and his colleagues used Eq. (3.1) to calculate scaled spectra for various experimental conditions, including different Mach and Reynolds numbers, as well as angles of attack. If the scaling function alone could account for noise variations due to these factors, then all the scaled levels for the different conditions would converge in a single scaled spectra. However, this was not the observed behavior. The scaled spectra did not converge into a single profile. Therefore, Brooks *et al.* introduced additional shape and amplitude functions to complement the scaling function and better match the experimental results.

The derivation of the spectral shape and amplitude functions was intended to model the measured scaled spectra based on variations in the free-stream velocities, Reynolds numbers, and angles of attack. The scaled spectra, according to Eq. (3.1), were initially modeled for scenarios with a zero angle of attack and varying free-stream velocities and Reynolds numbers. Two equations, including the scaling function from Ffowcs Williams and Hall and tuned shape and amplitude functions, were introduced to account for equal contributions of the pressure and suction sides to the total spectrum, assuming that each side of an airfoil produces TBL-TE noise independently. However, the shape and amplitude functions developed for a zero angle of attack were found to misrepresent the scaled spectral behavior in cases with varying angles of attack. Indeed, according to the zero angle of attack shape and amplitude functions, with an increasing angle of attack, the scaled peak Strouhal number would remain constant, the scaled peak level would decrease, and the scaled spectral shape would broaden at the peak. The experiments showed the opposite behavior. To compensate for this, Brooks, Pope, and Marcolini developed an additional angle-dependent noise component, using different shape and amplitude functions, which these authors referred to as “separated boundary layer noise contribution”. Although labeled as a “separated boundary layer noise contribution”, this component was intended to be active for non-zero angles of attack, including those well below the threshold for trailing edge separation

Thus, based on the BPM model, the total TBL-TE and separation noise spectrum in a 1/3-octave presentation is calculated, as detailed in Eq. (3.2), by adding the noise contributions at zero angle of attack from the pressure side (Eq. (3.3)) and the suction side (Eq. (3.4)), as well as the angle-dependent noise contribution (Eq. (3.5)).

$$\mathrm{SPL}_{\mathrm{TOT}} = 10\log(10^{\mathrm{SPL}_\alpha/10} + 10^{\mathrm{SPL}_s/10} + 10^{\mathrm{SPL}_p/10}) \tag{3.2}$$

$$\mathrm{SPL}_p = 10\log\left(\frac{\delta_p^* M^5 L \overline{D}_h}{r_e^2}\right) + A\left(\frac{\mathrm{St}_p}{\mathrm{St}_1}\right) + (K_1 - 3) + \Delta K_1 \tag{3.3}$$

$$\mathrm{SPL}_s = 10\log\left(\frac{\delta_s^* M^5 L \overline{D}_h}{r_e^2}\right) + A\left(\frac{\mathrm{St}_s}{\mathrm{St}_1}\right) + (K_1 - 3) \tag{3.4}$$

$$\mathrm{SPL}_\alpha = 10\log\left(\frac{\delta_s^* M^5 L \overline{D}_h}{r_e^2}\right) + B\left(\frac{\mathrm{St}_s}{\mathrm{St}_2}\right) + K_2 \tag{3.5}$$

The individual contributions to the total noise spectrum are determined by the aforementioned scaling function derived from the analysis by Ffowcs Williams and Hall *et al.* [13], spectral shape functions (A and B), and amplitude functions (K_1, K_2 and ΔK_1). Eq. (3.3), Eq. (3.4) and Eq. (3.5) incorporate the directivity function $\overline{D}_h$ as defined in [12]. The spectral shape functions depend on the ratio of the Strouhal numbers (St_p and St_s) to their peak values (St_1 and St_2) and the Reynolds number. Figure 3.2 depicts the shape function A, characterized by a concave downward parabolic shape that is symmetrical around $\mathrm{St}/\mathrm{St}_{\mathrm{peak}} = 1$. The width of this shape varies with the Reynolds number. Indeed, the shape functions are provided for both the maximum and minimum Reynolds numbers, as available from the experiments used to

develop this function. Interpolation is required to determine the shape function for any given Reynolds number.

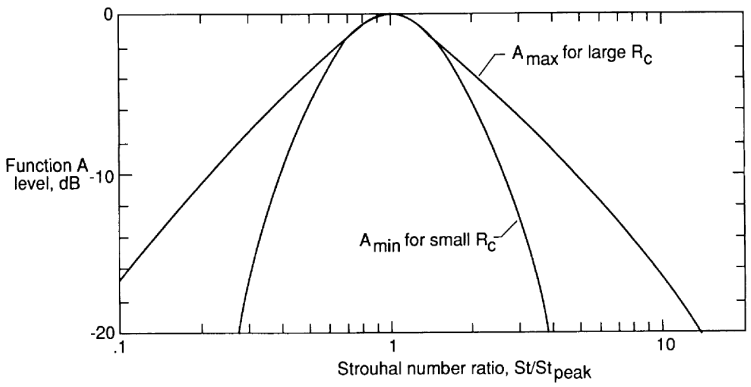

Figure 3.2: Spectral shapes A as functions of the ratio of the Strouhal number to its peak and Reynolds number. Image reproduced from Brooks *et al.* [12].

3.2 Validation against the BANC database

The Benchmark Problems for Airframe Noise Computations (BANC) database [2, 3, 4, 5] provides validation data for TBL-TE noise. The database include measurements from the Institute of Aerodynamics & Gas Dynamics (IAG) at the University of Stuttgart, DLR Braunschweig, the University of Florida (UFL) and Virginia Tech University (VTST). Table 3.1 summarizes the tested conditions. The NACA-0012 airfoil was utilized for the first four cases, the DU96-W-180 airfoil for case 5, and the NACA-64618 airfoil for cases 6 and 7. The boundary layer was tripped for cases 1 through 5, whereas cases 6 and 7 feature natural transition. Information on the tripping devices used for cases 1 through 5 is reported by Herr *et al.* [2].

Table 3.1: Tested airfoils and conditions in the BANC testcase.

case	airfoil	U [m s^{-1}]	AoA [°]	Re [-]
1	NACA-0012	56.0	0.00	$1.5 \cdot 10^6$
2	NACA-0012	54.8	4.00	$1.5 \cdot 10^6$
3	NACA-0012	53.0	6.00	$1.5 \cdot 10^6$
4	NACA-0012	37.7	0.00	$1.0 \cdot 10^6$
5	DU96-W-180	60.0	4.00	$1.1 \cdot 10^6$
6	NACA-64618	45.0	-0.88	$1.9 \cdot 10^6$
7	NACA-64618	45.0	4.62	$1.9 \cdot 10^6$

Figure 3.3 illustrates the influence of the Mach number's power on the scaled 1/3-octave spectra for cases 1 and 4. Both cases involve the same NACA-0012 airfoil and a zero angle of attack, differing only in the free-stream velocity. The scaled levels are calculated according to Eq. (3.1), with the exponent of the Mach number ranging from 4 to 7. The displacement thickness on the suction side, as estimated with RFOIL [14] under experimental conditions, is used for normalization. Figure 3.3 illustrates that a better collapse of the scaled levels is achieved using an exponent of five, confirming the Ffowcs Williams and Hall scaling function, as used in the BPM's TBL-TE noise model, is proportional to the fifth power of the Mach number.

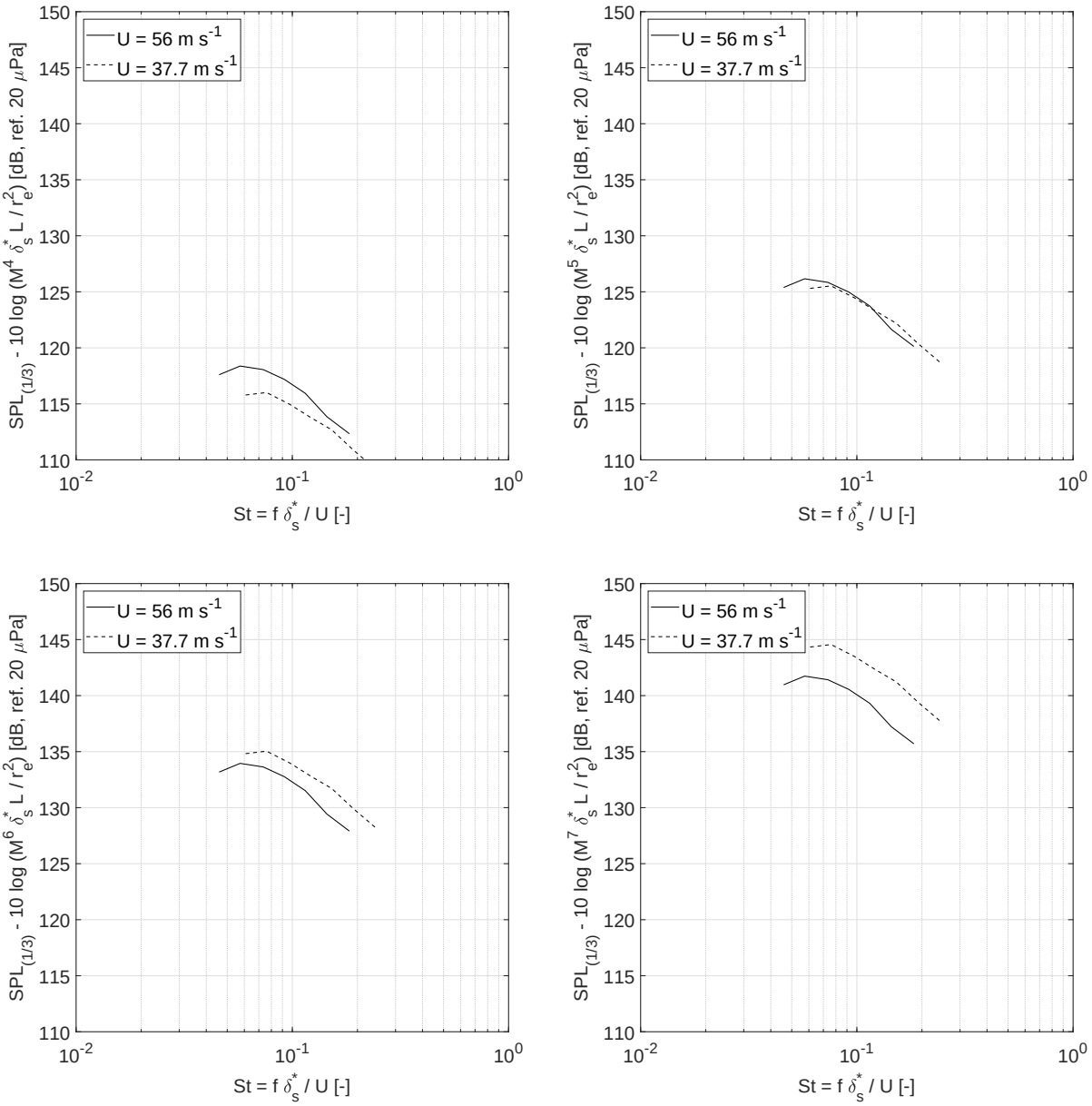

Figure 3.3: Scaled levels for BANC cases 1 and 4, both characterized by the same NACA-0012 airfoil and a zero angle of attack. Each plot is generated using a different scaling exponent for the Mach number (shown in the y-axis label of each plot).

Figure 3.4 presents the scaled 1/3-octave spectra for cases 1, 2, and 3. These cases involve the same airfoil and roughly the same free-stream velocity (see Table 3.1) but differ in their angles of attack. The fifth power of the Mach number and the displacement thickness on the suction side, as estimated with RFOIL under experimental conditions, are used for normalization. It is observed that as the angle of attack increases, the peak Strouhal number rises, the peak level decreases, and the spectral shape broadens at the peak. This behavior is not consistent to the one observed by Brooks and colleagues, which they modeled with the aforementioned additional angle-dependent noise component. Indeed, Brooks and colleagues observed that as the angle of attack increases, the peak level rises, and the spectral shape becomes less broad at the peak. To emphasize once more, this analysis was performed on scaled spectra

that already take into account Mach number and boundary layer thickness scaling.

Given that the behavior of scaled spectra for varying angles of attack differs between the BANC database and the BPM database, the BPM model should better align with the BANC cases when the angle-dependent noise contribution is excluded. To verify this, we examined the effect of including and excluding this contribution on the total sound pressure level using the BANC database.

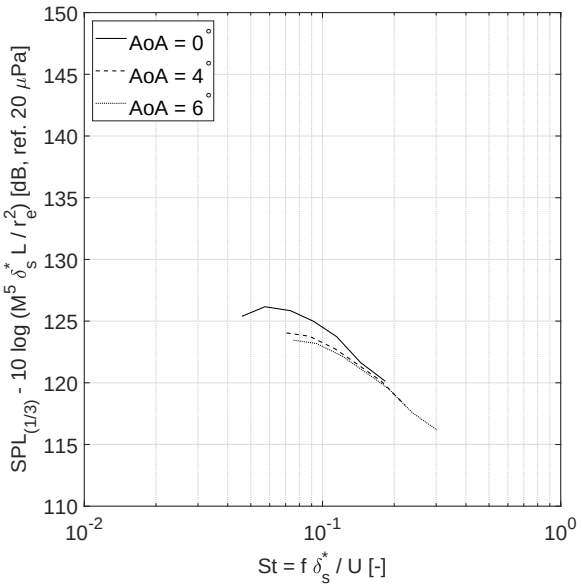

Figure 3.4: Scaled levels for BANC cases 1, 2, and 3, which involve the same NACA-0012 airfoil and approximately the same free-stream velocity, but with different angles of attack.

Figure 3.5 and Figure 3.6 show comparisons between the experimental and simulated sound pressure levels for BANC test cases 1 through 7. Simulations are performed using two codes that implement the BPM's TBL-TE noise model: SILANT [15] and NAFNoise [16]. For the SILANT simulations, the required boundary layer displacement thicknesses are predicted using RFOIL, prescribing the experimental condition. This implies an amplification factor 'Ncrit' of 9, and the specified chordwise transition location on pressure and suction side (Case 1 to 5) or free transition (Case 6 and 7). The BANC database includes the results of NAFNoise simulations for the specified test cases. We utilized these results to verify the consistency of our SILANT setup. For both SILANT and NAFNoise, we present the predicted total noise, including and excluding the angle-dependent noise component. The results without the angle-dependent noise component are labeled as "noSPLalpha". It is observed that the angle-dependent noise component results in an overestimation of the noise level (up to 5 dB) for the BANC cases with non-zero angles of attack. Better agreement is indeed achieved by omitting this component for cases 2, 3, and 7. In case 5, the experimental spectrum does not include the peak, making it impossible to assess whether the exclusion of the angle-dependent noise component led to better results.

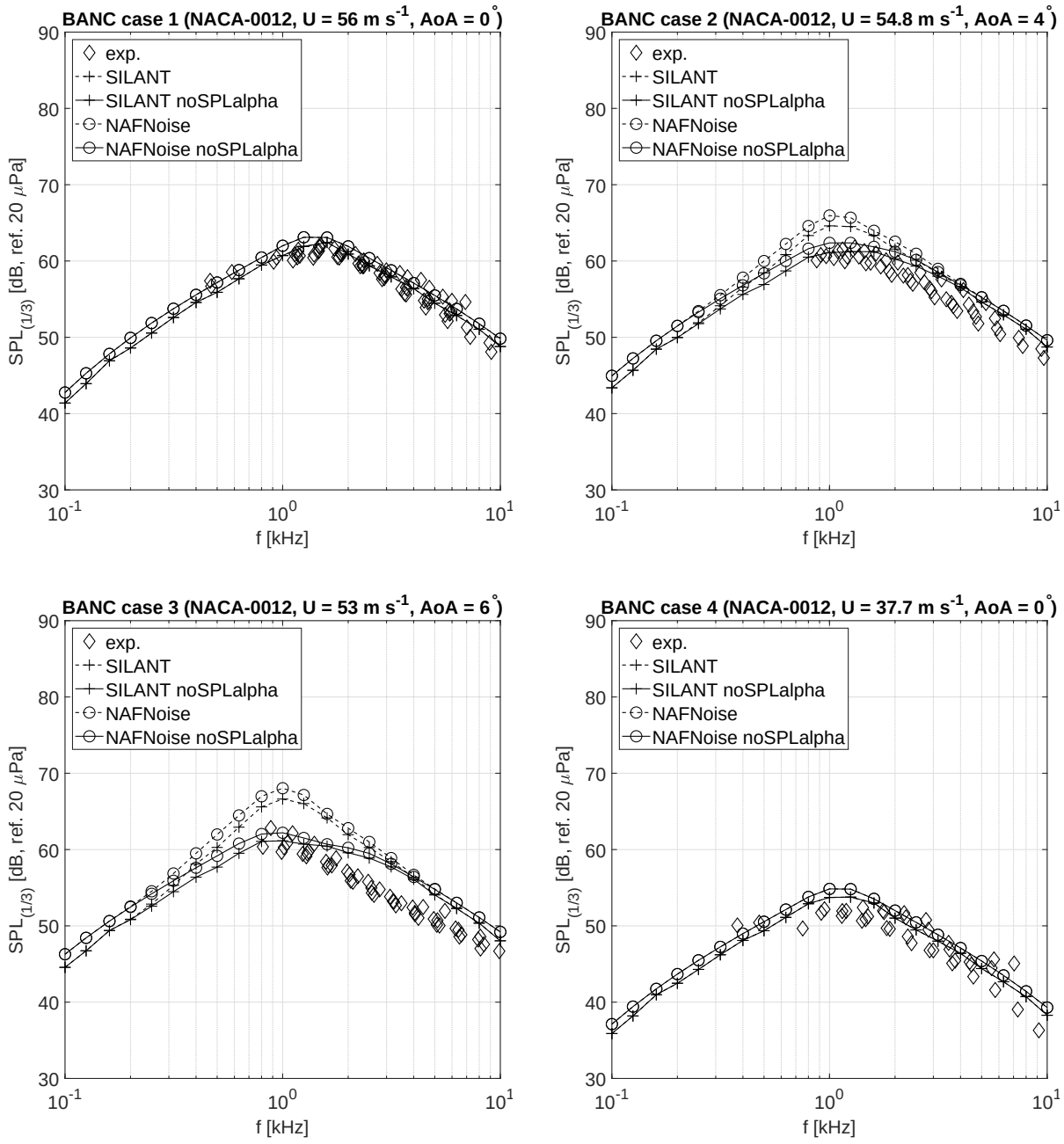

Figure 3.5: Comparison between experimental and simulated 1-3-octave band sound pressure level for BANC case 1, 2, 3 and 4. The figures presents measurements from IAG, DLR and UFL which were combined together.

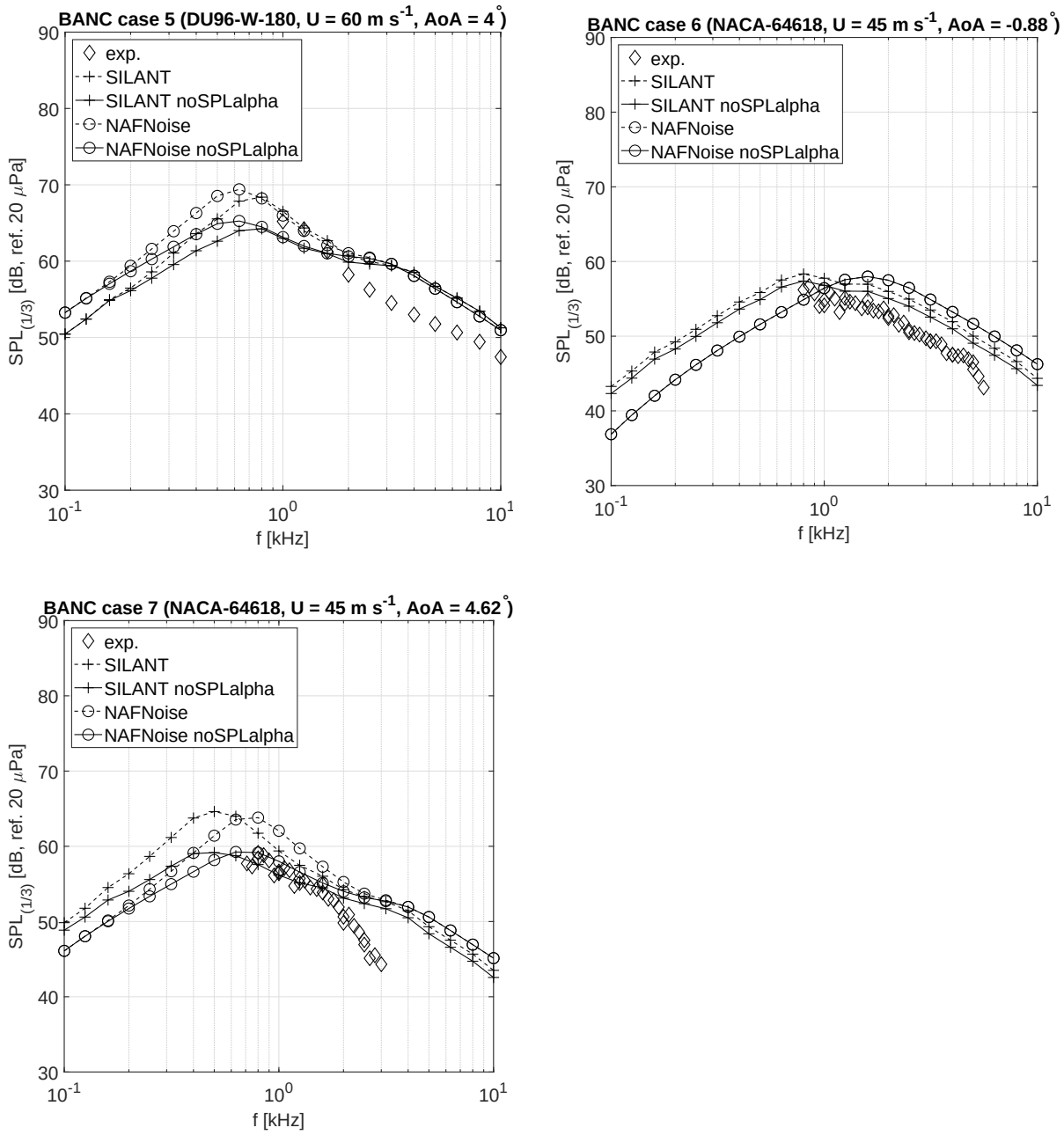

Figure 3.6: Comparison between experimental and simulated 1-3-octave band sound pressure level for BANC case 5, 6 and 7. The figures presents measurements from DLR for case 5 and from VTST for case 6 and 7.

Figure 3.7 presents the overall sound pressure levels for BANC cases 1 to 5. Omitting the angle-dependent noise component results in better agreement for all cases.

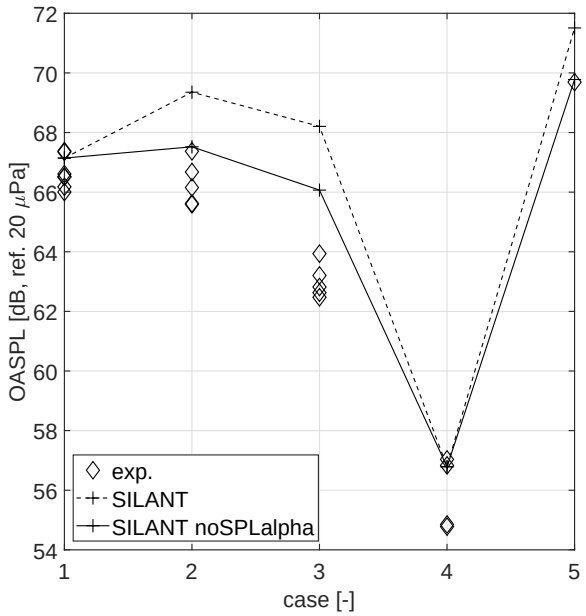

Figure 3.7: Overall sound pressure levels for BANC cases 1 to 5.

3.3 Validation against the A-tunnel NACA-0018 database

Within the BEST project, several noise measurements were performed in the A-tunnel of TU-Delft [17], featuring a NACA-0018 profile. The set-up is similar to the one described in [18] as illustrated in Figure 3.8.

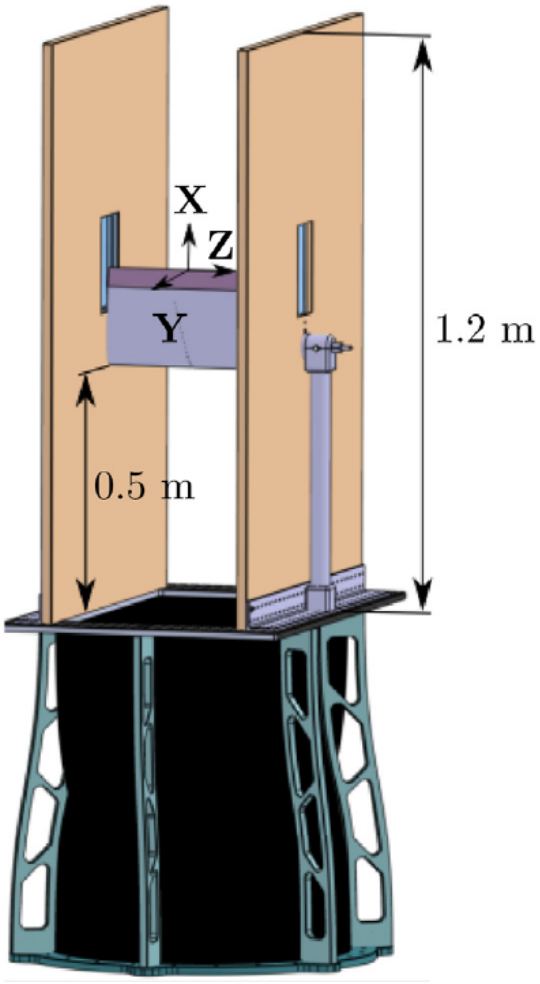

Figure 3.8: Test set-up in the A-tunnel, image taken from [18].

Table 3.2 summarizes the test conditions from the A-tunnel NACA-0018 database, taken March 2024, used for this validation. The NACA-0018 airfoil was tested at the same free-stream velocity with increasing angles of attack, both with and without the trailing edge add-on. The boundary layer was tripped with ZZ-tape at 10% chord (pressure side) and 5% chord (suction side). This section focuses on the results obtained for the nominal configuration, while the figure includes results concerning the add-on configuration as well, which will be referenced throughout the remainder of the report.

Table 3.2: Tested airfoils and conditions in the A-tunnel database (March 2024).

case	airfoil	U [m s^{-1}]	AoA [°]	Re [-]
1	NACA-0018	20	0	$0.263 \cdot 10^6$
2	NACA-0018	20	2	$0.263 \cdot 10^6$
3	NACA-0018	20	4	$0.263 \cdot 10^6$
4	NACA-0018	20	6	$0.263 \cdot 10^6$
5	NACA-0018	20	8	$0.263 \cdot 10^6$
6	NACA-0018	20	10	$0.263 \cdot 10^6$

Figures 3.9 and 3.10 present comparisons between the experimental and simulated sound pressure levels for angles of attack from zero to ten degrees. Simulations are performed using SILANT. The required boundary layer displacement thicknesses are predicted using RFOIL, prescribing the experimental condition. This implies an amplification factor 'Ncrit' of 9, and the specified chordwise transition location on pressure and suction side corresponding to the trip strip location. The predicted total noise, both including and excluding the angle-dependent noise component, is shown. The results without the angle-dependent noise component are labeled as 'noSPLalpha'. It is observed that the angle-dependent noise component leads to an overestimation of the noise level for cases with non-zero angles of attack. As seen with the BANC cases, better agreement is achieved by omitting this component.

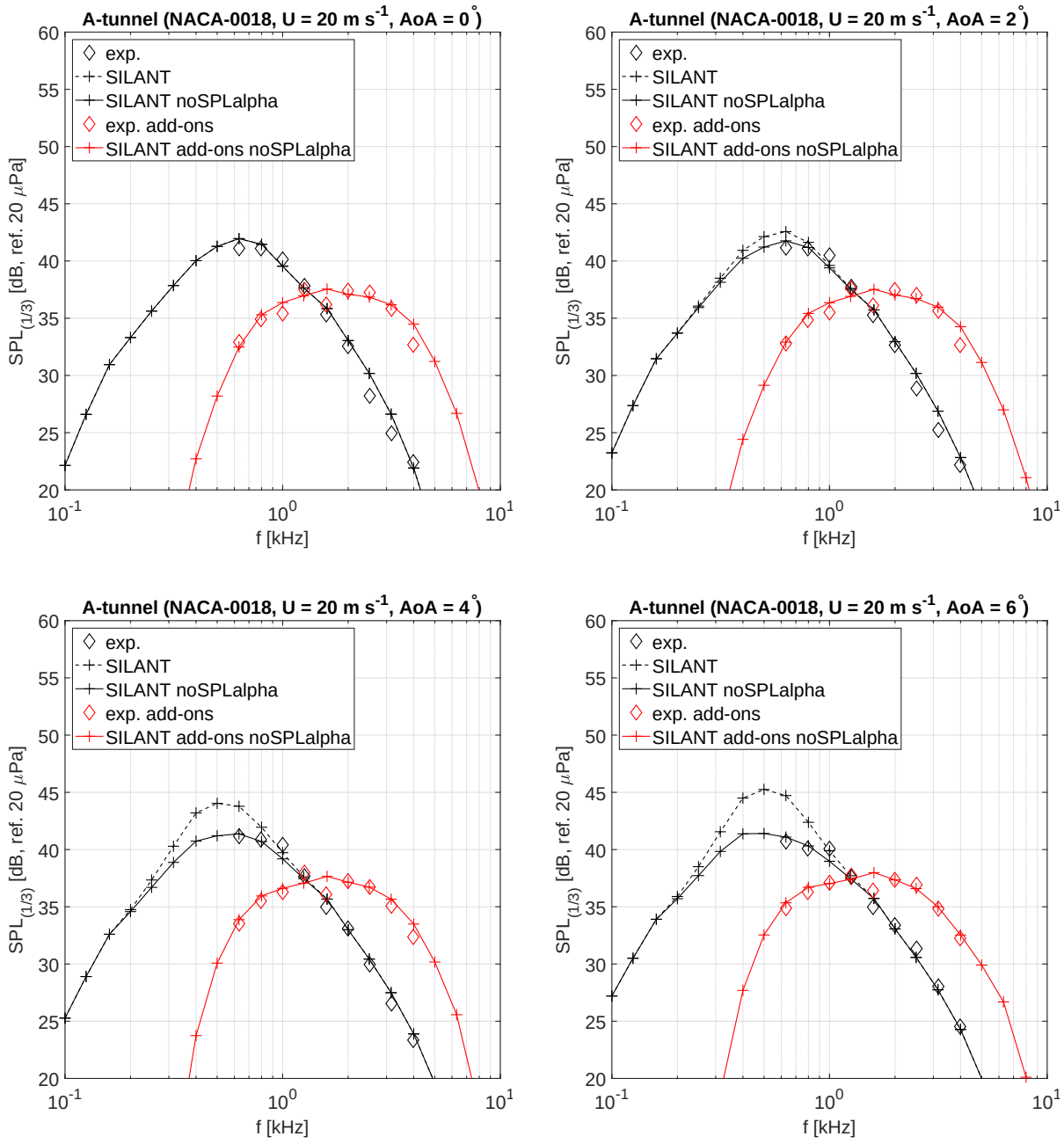

Figure 3.9: Comparison of measured and simulated 1/3-octave spectra for the nominal NACA-0018 airfoil and the NACA-0018 airfoil featuring trailing edge noise mitigation add-ons at angles of attack from 0° to 6° and a free-stream velocity of 20 m s^{-1}.

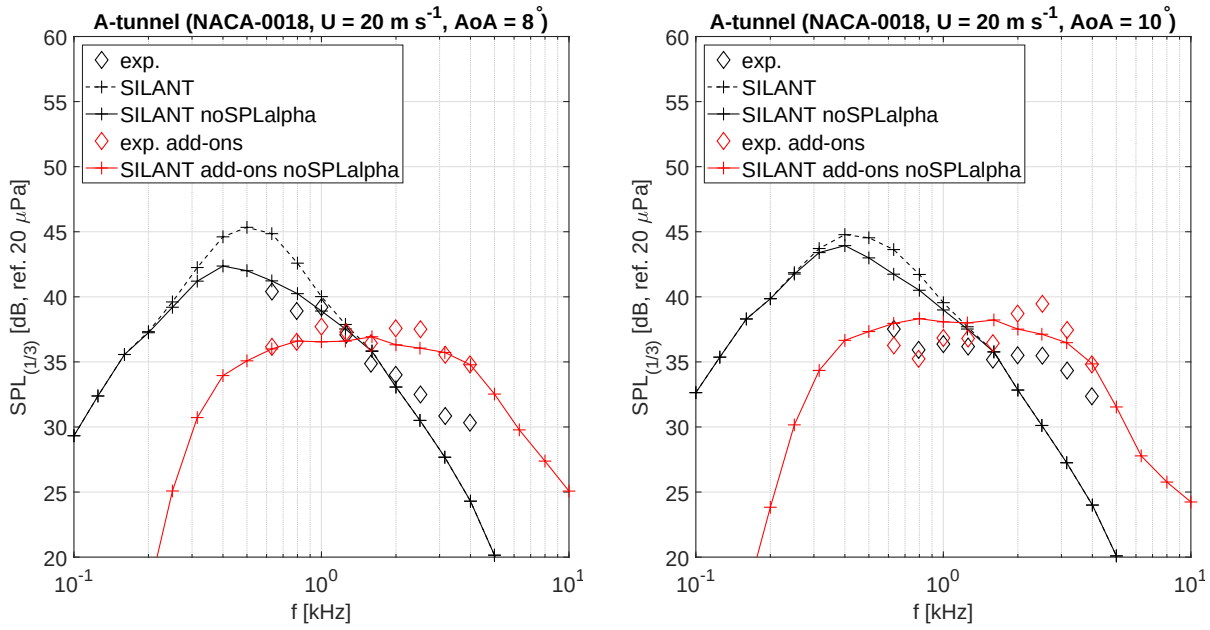

Figure 3.10: Comparison of measured and simulated 1/3-octave spectra for the nominal NACA-0018 airfoil and the NACA-0018 airfoil featuring trailing edge noise mitigation add-ons at angles of attack from 7.8° to 10° and a free-stream velocity of 20 m s^{-1}.

3.4 Validation against the Poul la Cour Tunnel FFA-W3-211 database

For tests at larger Reynolds numbers, more representative for full scale conditions on wind turbines, wind tunnel tests were performed in the Poul La Cour Tunnel in Denmark [19] using the FFA-W3-211 profile in December 2024. Similar to the tests at the A-tunnel, the tests were performed for both a nominal airfoil and a modification featuring trailing edge mitigation add-ons. The test set-up is depicted in Figure 3.11, with a summary of the tested conditions in Table 3.3.

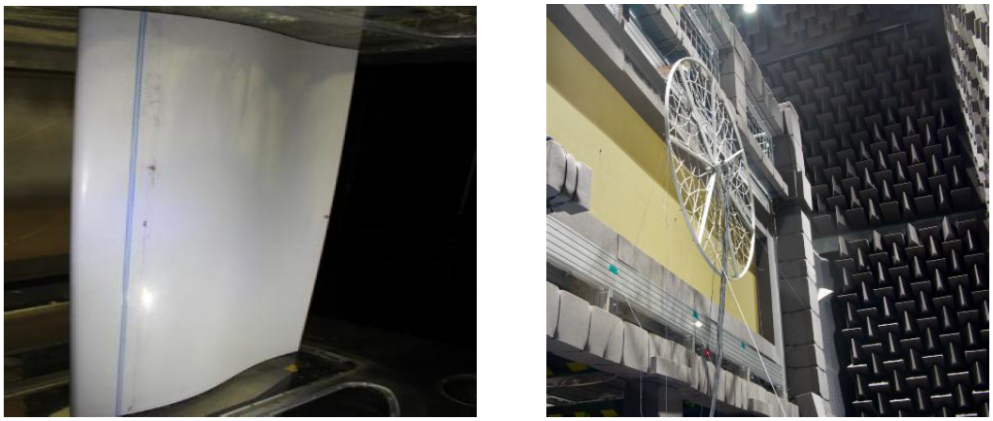

Figure 3.11: Test set-up in the Poul la Cour tunnel, image taken from [20]. Left: Airfoil profile. Right: Microphones and anechoic chamber

Table 3.3: Tested airfoil and selected conditions in the Poul La Cour Tunnel database (December 2024).

case	airfoil	U [m s^{-1}]	AoA [°]	Re [-]
1	FFA-W3-211	30	0	$1.9 \cdot 10^6$
2	FFA-W3-211	50	0	$3.1 \cdot 10^6$
3	FFA-W3-211	80	0	$4.9 \cdot 10^6$
4	FFA-W3-211	30	4	$1.9 \cdot 10^6$
5	FFA-W3-211	50	4	$3.1 \cdot 10^6$
6	FFA-W3-211	80	4	$4.9 \cdot 10^6$
7	FFA-W3-211	30	6	$1.9 \cdot 10^6$
8	FFA-W3-211	50	6	$3.1 \cdot 10^6$
9	FFA-W3-211	80	6	$4.9 \cdot 10^6$

The boundary layer was tripped at 10% chord (pressure side) and 5% chord (suction side) using 0.4 mm thick ZZ-tape.

Simulations are performed using SILANT for thee different angles of attack, $0°$, $4°$ and $6°$. The required boundary layer displacement thicknesses are predicted using RFOIL, prescribing the experimental condition. This implies an amplification factor 'Ncrit' of 9, and the specified chord-wise transition location on pressure and suction side corresponding to the trip strip location. The simulation results are compared to the measurements in Figure 3.12, 3.13 and 3.14.

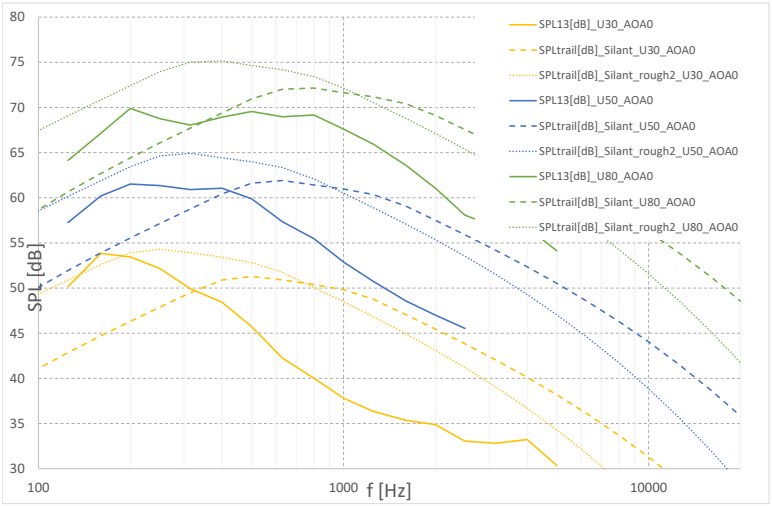

Figure 3.12: Comparison of measured and predicted 1/3-Octave band spectra of the FFA-W3-211 profile at 0° angle of attack in the PLC tunnel for 30 m/s (yellow), 50 m/s (blue) and 80 m/s (green). Measurements (solid line) are compared against SILANT simulations (dashed). To mimick the effect of additional roughness, a simulation has been performed doubling the boundary layer displacement thickness (dotted).

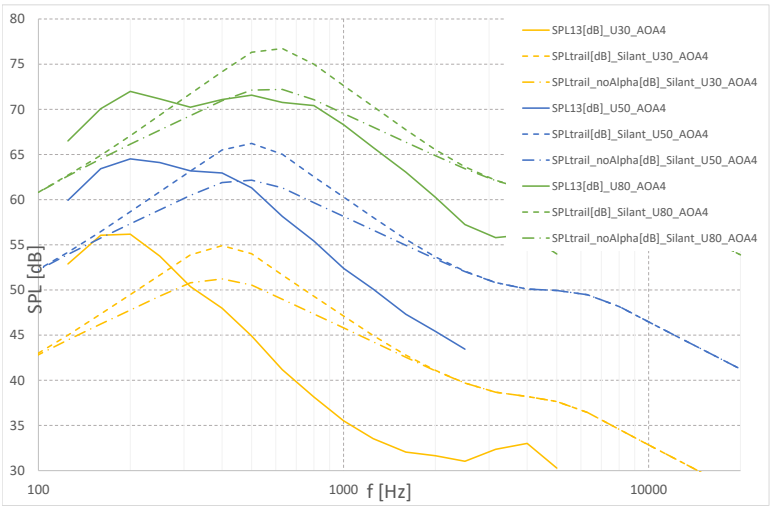

Figure 3.13: Comparison of measured and predicted 1/3-Octave band spectra of the FFA-W3-211 profile at 4° angle of attack in the PLC tunnel for 30 m/s (yellow), 50 m/s (blue) and 80 m/s (green). Measurements (solid line) are compared against SILANT simulations with (dashed) and without (dash-dot) SPLalpha contribution.

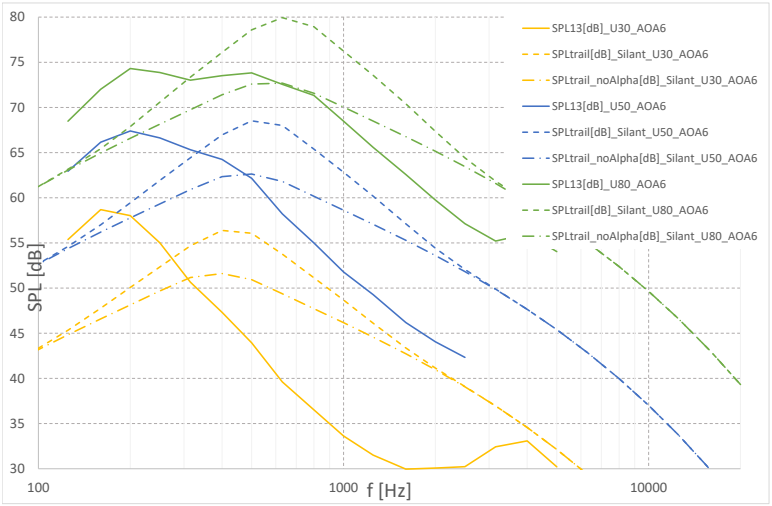

Figure 3.14: Comparison of measured and predicted 1/3-Octave band spectra of the FFA-W3-211 profile at 6° angle of attack in the PLC tunnel for 30 m/s (yellow), 50 m/s (blue) and 80 m/s (green). Measurements (solid line) are compared against SILANT simulations with (dashed) and without (dash-dot) SPLalpha contribution.

A striking observation for all wind speeds and angles of attack is the consistent over prediction of the peak frequency by the BPM model, by about a factor of 3. Based on the relatively good agreement in the validation sections above, and judging by the results of previous validation exercises [21], the magnitude of the discrepancy is unexpected. In search of possible causes, it is noted that the profile of investigation is an FFA profile, while the BPM model scaling has been based on NACA type profiles. Acknowledging the scaling of peak frequency with the boundary layer displacement thickness, the effect of tripping is also considered. Traditionally, the required height of roughness elements for transition can be estimated using the method of Braslow and Knox [22], based on the critical Reynolds number (referenced to the roughness height) for a flat plate with grit roughness. For the current conditions, the required height is estimated less than 0.2 mm (which is considerably lower than the 0.4 mm thickness used here), even considering the negative pressure gradient on the nose and the application of a zigzag instead of grit type roughness. Hence this could point in the direction of over tripping, which is known to promote a larger boundary layer thickness. However in that case the noise level of the peak should scale along as well. To investigate this further, the boundary layer displacement thicknesses have been doubled by means of an experiment for the 0° angle of attack case in Figure 3.12 (dotted lines). Although the peak frequencies are in better agreement, the levels for the 4° and 6° angles of attack seem over predicted. Hence further investigation is necessary to arrive at more solid conclusions. Because the cause for the discrepancy is yet unclear, and hence the reference spectra are uncertain, the database was not used to tune the modification of the BPM model as described in Chapter 4.

4 Modification of the BPM model for trailing edge noise mitigation add-ons

4.1 Modification methodology

Wind turbine noise is a disadvantage that hinders the deployment of onshore wind turbines. Regulations are in place to limit people's exposure to this noise. To comply with these regulations, wind turbine operators often reduce rotor speed, which decreases noise but also lowers energy production. To enhance the commercial appeal of their turbines, manufacturers must consider noise during the design phase, balancing performance and noise emission. The boundary layer turbulence passing the trailing edge is considered the primary noise source for wind turbine applications [23]. To further improve noise reduction, various trailing edge add-ons, including serrations, brushes, fences and extensions with permeable and elastic materials, have been developed [24]. The design of wind turbine blades depends on fast engineering methods that model blade noise, including trailing edge noise reduction add-ons.

For conventional blades, noise modeling ranges from simple empirical one-equation models to computational aeroacoustic simulations that capture both the flow field and acoustic disturbances around wind turbine blade [25]. A balance between accuracy and computational effort can be achieved with semi-empirical methods, which segment wind turbine blades and treat them as two-dimensional airfoil sections that generate sound sources [15, 26]. The Brooks, Pope, and Marcolini (BPM) model [12] is the most widely used in industrial practice for predicting these sectional sources. Brooks and colleagues developed semi-empirical models to predict airfoil self-noise, utilizing both theoretical studies and acoustic measurement data. The modeled noise mechanisms encompassed turbulent boundary layer trailing edge (TBL-TE) noise, laminar boundary layer vortex shedding noise, separation stall noise, trailing edge bluntness vortex shedding noise, and tip vortex formation noise.

Only a limited number of studies have explored quick engineering modeling techniques for trailing edge mitigation add-ons. Notably, Mayer *et al.* [27] and Lyu and Ayton [28] developed rapid noise prediction models for serrated trailing edges using new analytical formulations. Wang *et al.* [29] developed a semi-empirical model for predicting rotor noise, which includes blade add-ons. The model relies on spectral corrections that were calibrated using wind and field measurements, as well as computational aeroacoustics simulations.

This section aims to present a straightforward method for modifying the widely used BPM model to incorporate the effects of generic trailing edge noise mitigation add-ons for wind turbine blades, for which wind tunnel data is available. The methodology involves fine-tuning certain BPM parameters to align the model output with wind tunnel data.

4.1.1 Parameterization

The aim of this work is to largely retain the equation structure of the BPM's TBL-TE noise model, developed for conventional airfoil shapes, and adjust some of its parameters to

model the noise of airfoils with noise mitigation add-ons. As explained in the validation section reported below, we found that better results are obtained by omitting the aforementioned angle-dependent noise contribution. Therefore, Eq. (3.5) was excluded from the equation structure, relying solely on Eq. (3.3) and Eq. (3.4).

The BPM's TBL-TE noise model defines the spectral shape using shape functions, such as the one shown in Figure 3.2. This spectral shape was empirically determined using measurements on a conventional airfoil. To capture the spectral shapes of airfoils with noise mitigation add-ons, we modified the original spectral function by defining an alternative spectral function using Eq. (4.1):

$$A = -20\left(\log\left(\frac{\mathrm{St}}{\mathrm{St}_{\mathrm{peak}}}\right)I^{-1}\right)^{e} \tag{4.1}$$

where I is the value of $\mathrm{St}/\mathrm{St}_{\mathrm{peak}}$ at A = -20 dB, and e is the function's exponent. This formula was devised by the authors and found to accurately represent the original spectral function by adjusting its parameters I and e. Thus the spectral function in parameterized by means the parameters e and I. Figure 4.1 compares the original spectral function to the parameterized one. As mentioned above, the original BPM's TBL-TE noise model extrapolates the spectral function for the actual Reynolds number using two empirical spectral functions, A_{max} and A_{min}, respectively determined for the maximum Reynolds number and the minimum Reynolds number. Figure 4.1 shows the shape functions at the maximum and minimum Reynolds numbers, the interpolated shape function at a given Reynolds number, and the parameterized shape function determined to match the interpolated function as closely as possible. The comparison demonstrates that the parametric spectral function has good flexibility and effectively captures the original function. To capture the noise of airfoils with trailing edge add-ons, the

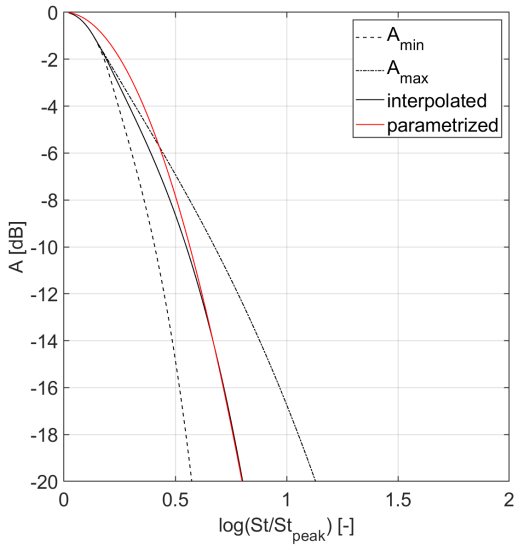

Figure 4.1: Spectral shape functions at the maximum and minimum Reynolds numbers, A_{max} and A_{min}, the interpolated shape function at a given Reynolds number, and the parameterized shape function.

spectral shape alone is not sufficient. The spectral peak Strouhal number and level also need to be modeled. The spectral peak Strouhal number St_1 is directly a parameter in Eq. (3.3) and Eq. (3.4). The level is adjusted using the K_1 parameter, which in the original model is a function of the Reynolds number and also appears in Eq. (3.3) and Eq. (3.4). Since St_1 and K_1 are direct model parameters and the parametric spectral function can closely matches the original, as shown in Figure 4.1, the parametrization, with proper tuning of the parameters, is able to align with the original BPM model.

In summary, the proposed modification of the BPM's TBL-TE noise model is based on four parameters: e, I, St_1 and K_1. Figure 4.2 illustrates the individual impact of these parameters on the predicted sound pressure level using a generic test case. The parameters e and I affect the broadness of the spectrum around its peak and the slope of the spectrum towards its peak. The parameter St_1 shifts the spectrum in the frequency direction (i.e., along the x-axis), while K_1 shifts it in the sound pressure level direction (i.e., along the y-axis).

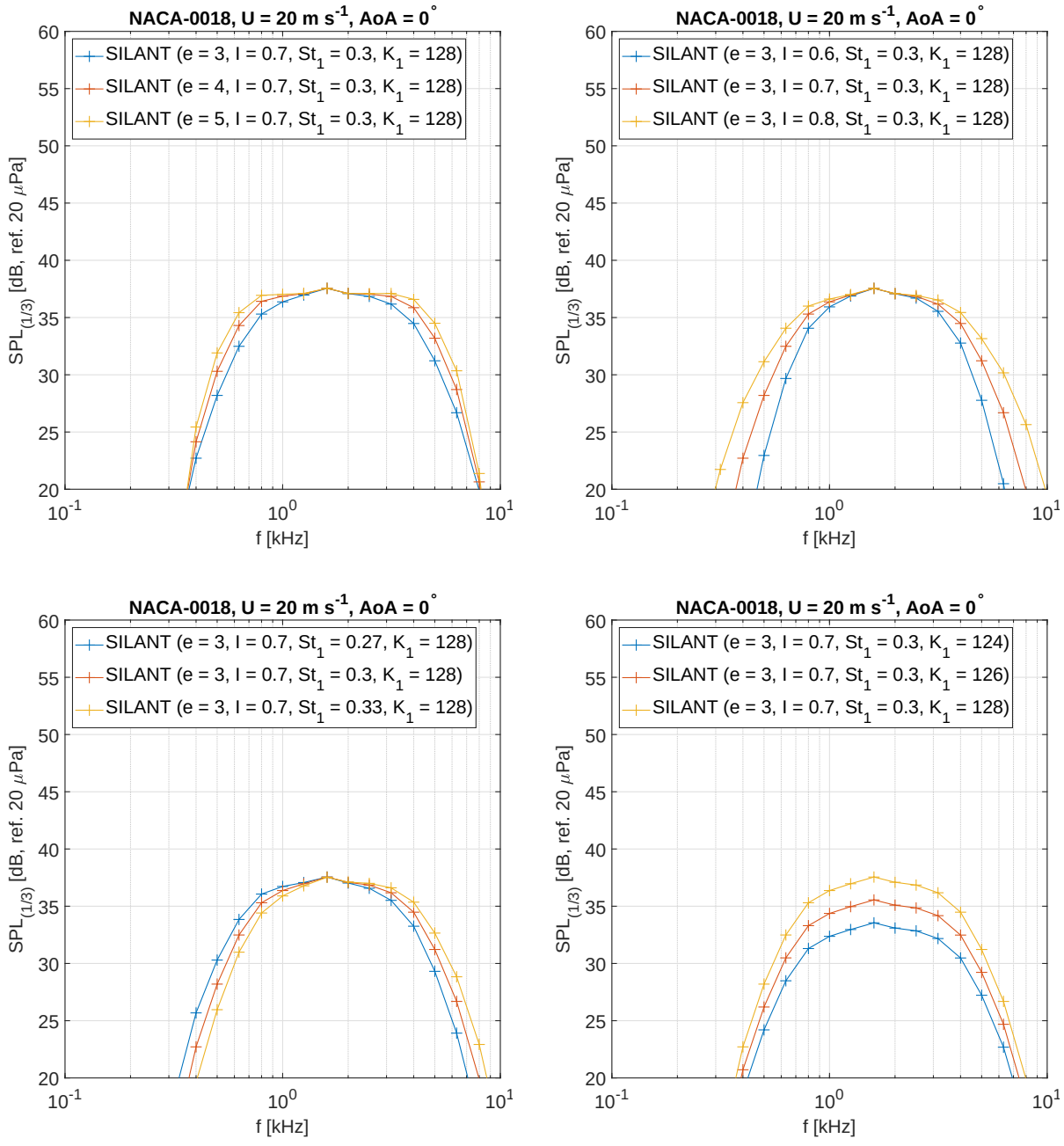

Figure 4.2: Individual impact of parameters e, I, St_1 and K_1 on the predicted sound pressure level.

4.1.2 Modification

In this section, we present the modification of the original BMP model to include the trailing edge noise mitigation of an undisclosed MuteSkin add-on configuration, which was applied to the nominal NACA-0018 profile and acoustically measured in the A-tunnel at TU Delft. During the same campaign, measurements were also conducted on the nominal NACA-0018 airfoil. Figure 4.3 shows the scaled spectra from measurements of the nominal airfoil and one with the trailing edge noise mitigation add-ons. Because the trailing edge boundary layer displacement thickness remains unaffected by the add-ons, RFOIL is utilized to determine this thickness for both the nominal airfoil and the one with add-ons. In both cases, as the angle of attack increases, the peak Strouhal number rises, the peak level decreases, and the spectral shape broadens at the peak. This behavior is consistent with the observations reported above for the BANC cases.

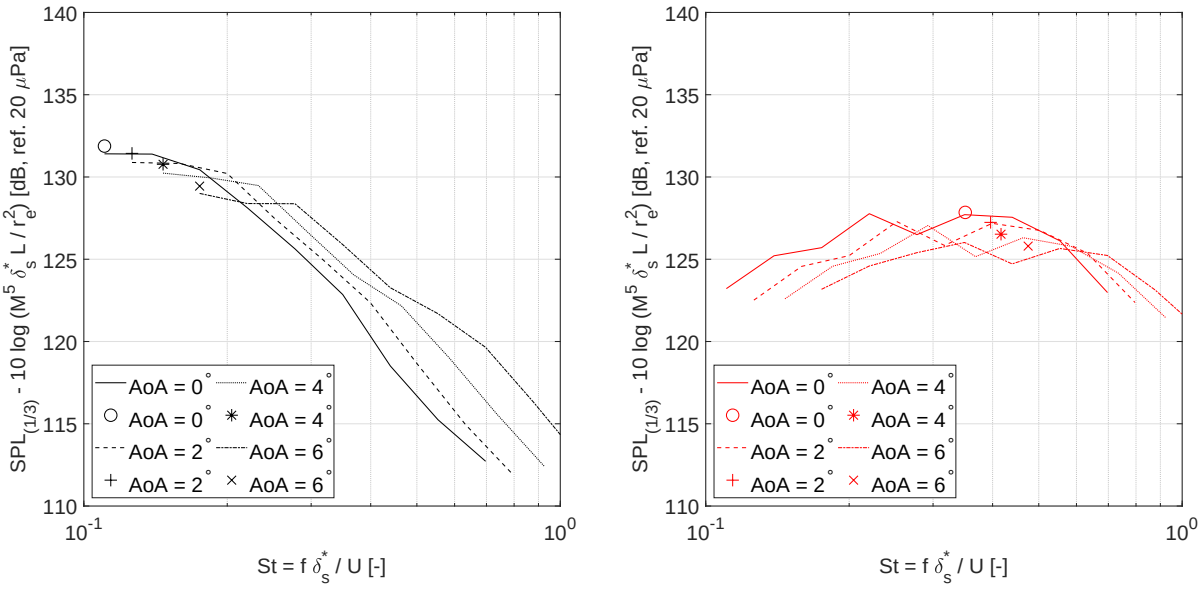

Figure 4.3: Scaled 1/3-octave spectra for airfoils at different angles of attack and a free-stream velocity of 20 m s^{-1} are shown for the nominal NACA-0018 airfoil (left subplot) and the NACA-0018 airfoil with trailing edge noise mitigation add-ons. The lines represent measured spectra, while markers indicate the approximate spectral peak locations.

Figures 3.9 and 3.10 present comparisons between the experimental and simulated sound pressure levels for angles of attack from zero to ten degrees. Simulations are performed using SILANT. The predicted total noise, both including and excluding the angle-dependent noise component, is shown. The results without the angle-dependent noise component are labeled as 'noSPLalpha'. It is observed that the angle-dependent noise component leads to an over-estimation of the noise level for cases with non-zero angles of attack. As seen with the BANC cases, better agreement is achieved by omitting this component.

The four previously mentioned parameters were adjusted to closely match the measured 1/3-octave spectra of the airfoil with trailing edge noise mitigation add-ons to the modeled spectra. Figures 3.9 and 3.10 illustrate the strong agreement between the experimental and simulated spectra for airfoils with noise mitigation add-ons (in red colour), achievable through parameter tuning. Figure 4.4 shows the values of the model parameters as a function of the angle of attack. The experiment demonstrates that as the angle of attack increases, the spectral shape

broadens, which is reflected by the rising values of e and I. The increase in peak frequency is captured by the rise in St_1, while the reduction in level is achieved through the reduction in K_1.

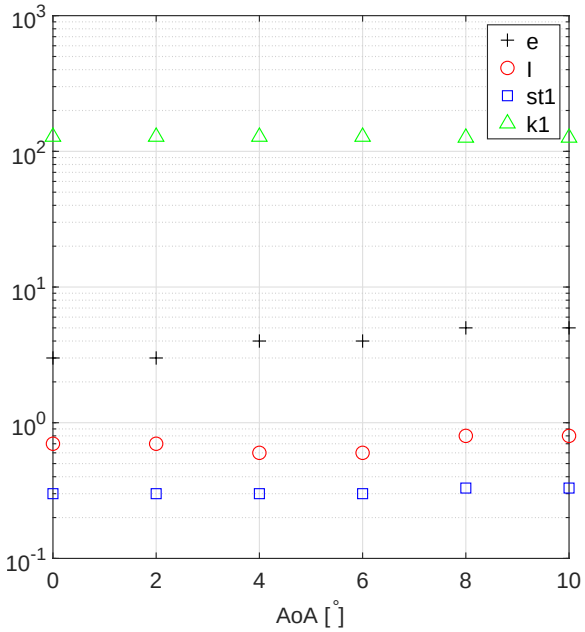

Figure 4.4: Values of BPM parameters as a function of the angle of attack.

4.2 Application to rotor simulations

To illustrate the effect of the adapted model for blade extensions, a full rotor simulation was performed using the modified SILANT code. The ART 5MW turbine [30], which is based on the NREL 5MW turbine [31] featuring a redesigned rotor, is chosen as a representative turbine for onshore applications. See also table 4.1 for the main specifications of this turbine. The turbine is modelled rigid for this purpose. An operational condition in the so-called knee of

Table 4.1: Summary of main specifications of the ART 5MW turbine.

Parameter	Unit	Value
Rotor diameter	[m]	128.4
Hub height	[m]	90
Rated power	[MW]	5
Rated rotor speed	[rpm]	12.393
Rated tip speed	[m/s]	83.3
Control	[-]	Variable speed, collective pitch
Rotor orientation	[-]	upwind
Nuber of blades	[-]	3
Tilt angle	[deg]	5
Cone angle	[deg]	-2.5

the power curve is investigated, where the noise source levels peak at a wind speed of 10.5 m/s around rated rotor speed and zero pitch angle. Both a reference simulation as well as a simulation with the outer 30% of the blade span treated with a porous blade extension has been performed. For the latter, the modification to SILANT as described in section 4.1.2 has been used. The resulting noise spectra are illustrated in Figure 4.5 for the various calculated noise sources (trailing edge turbulent boundary layer noise, inflow noise and tip noise). Here

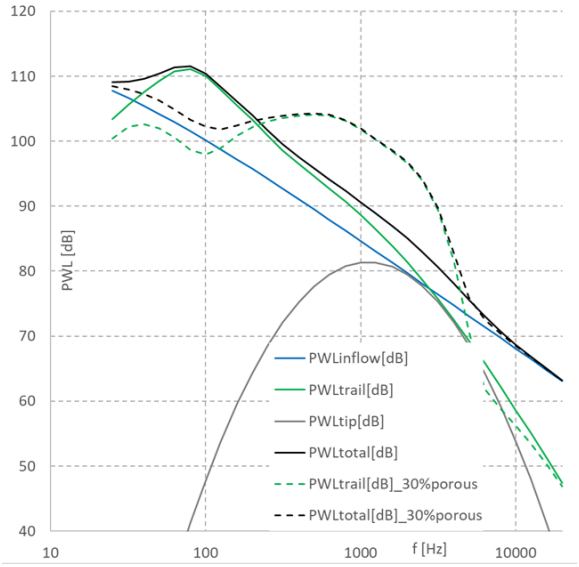

Figure 4.5: Unweighted noise power spectra for the reference (solid) and last 30% span treated simulation (dashed), ART 5MW rotor at 10.5 m/s hub height wind speed.

it becomes clear that, similar to the wind tunnel results as shown in Figures 3.9 and 3.10, the trailing edge noise peak level is decreased and shifts to a higher frequency. As a result, the corresponding overall noise source levels are predicted to decrease by 2.4 dB. It is noted that, depending on the noise distribution over the frequency range, the effect of A-weighting could change the overall sound power levels and the difference between them. Also, it should be emphasized that, since the modification was tuned for Reynolds numbers in the order of 10^5, the validity of applying this model to real life Reynolds numbers an order of magnitude larger remains questionable. Therefore the above presented results should be interpreted with care, and only serve to obtain a qualitative idea about the impact on a full rotor simulation.

5 Conclusions

Reynolds-Averaged Navier-Stokes (RANS) simulations indicate that the boundary layer, and consequently the aerodynamic conditions, of an airfoil equipped with porous trailing edge noise mitigation add-ons, like MuTech's MuteSkin, does not significantly differ from that of the same airfoil without these add-ons. Additionally, it has been observed that RANS simulations are insufficient for capturing the mechanisms responsible for noise reduction, leading to the decision to discontinue further research in this area.

Conversely, a very positive result was found for the modification of an engineering noise prediction model, originally designed for conventional airfoils, to include the effects of trailing edge noise mitigation add-ons. By adjusting its parameters, we successfully adapted the well-known turbulent boundary layer trailing edge noise model by Brooks *et al.*. We tuned the model parameters to match the model output with the acoustic measurement data obtained from airfoils equipped with MuTech add-ons. The acoustic dataset we used to adjust Brooks *et al.* model for trailing edge noise mitigation add-ons was limited, allowing us to investigate only variations due to changes in the angle of attack. Future work should aim to create a more comprehensive measurement dataset that includes free-stream velocity and the geometrical features of the add-ons.

References

[1] Marco Caboni, Koen Boorsma, and Akshay Koodly Ravishankara. “Adjustments to Brooks, Pope, and Marcolini’s model to incorporate trailing edge noise mitigation add-ons for wind turbine blades”. In: *Proceedings of the 11th Edition of International Conferences on Wind Turbine Noise*. Copenhagen, Denmark, June 2025.

[2] Michael Herr and Md Kamruzzaman. “Benchmarking of Trailing-Edge Noise Computations: Outcome of the BANC-II Workshop”. In: *19th AIAA/CEAS Aeroacoustics Conference*. American Institute of Aeronautics and Astronautics. 2013, p. 2123. DOI: 10.2514/6.2013-2123.

[3] Michael Herr et al. “Broadband Trailing-Edge Noise Predictions—Overview of BANC-III Results”. In: *21st AIAA/CEAS Aeroacoustics Conference*. American Institute of Aeronautics and Astronautics. 2015, p. 2847. DOI: 10.2514/6.2015-2847.

[4] Michaela Herr, Mohammad Kamruzzaman, and Christopher J. Bahr. “Fourth Workshop on Benchmark Problems for Airframe Noise Computations (BANC-IV); Category 1: Trailing-Edge Noise”. In: 2014. URL: https://api.semanticscholar.org/CorpusID:60274133.

[5] Meelan Choudhari and David P Lockard. “Simulations & Measurements of Airframe Noise: A BANC Workshops Perspective”. In: 2016. URL: https://api.semanticscholar.org/CorpusID:113690679.

[6] Brian D Wood, Xiaoliang He, and Sourabh V Apte. “Modeling turbulent flows in porous media”. In: *Annual Review of Fluid Mechanics* 52.1 (2020), pp. 171–203.

[7] Stephen Whitaker. “Flow in porous media I: A theoretical derivation of Darcy’s law”. In: *Transport in porous media* 1 (1986), pp. 3–25.

[8] Henry G Weller et al. “A tensorial approach to computational continuum mechanics using object-oriented techniques”. In: *Computers in physics* 12.6 (1998), pp. 620–631.

[9] Haukur Elvar Hafsteinsson. “Porous media in OpenFOAM”. In: *Chalmers University of Technology, Gothenburg* (2009).

[10] C. Teruna et al. “Noise reduction mechanisms of an open-cell metal-foam trailing edge”. In: *Journal of Fluid Mechanics* 898 (2020), A18. DOI: 10.1017/jfm.2020.363.

[11] C. Teruna et al. “On the noise reduction of a porous trailing edge applied to an airfoil at lifting condition”. In: *Physics of Fluids* 33.5 (2021), p. 055132.

[12] Thomas F. Brooks, D. Stuart Pope, and Michael A. Marcolini. *Airfoil Self-Noise and Prediction*. Tech. rep. NASA-RP-1218. NASA Langley Research Center, 1989. URL: https://ntrs.nasa.gov/api/citations/19890016302/downloads/19890016302.pdf.

[13] J. E. Ffowcs Williams and L. H. Hall. “Aerodynamic sound generation by turbulent flow in the vicinity of a scattering half plane”. In: *Journal of Fluid Mechanics* 40.4 (1970), pp. 657–670. DOI: 10.1017/S0022112070000368.

[14] R.P.J.O.M A. van Rooij. *Modification of the boundary layer calculation in RFOIL for improved airfoil stall prediction*. Tech. rep. IW-96087R. TU Delft, 1996.

[15] K. Boorsma and J.G. Schepers. “Enhanced wind turbine noise prediction tool SILANT”. In: *Proceedings of the Fourth International Meeting on Wind Turbine Noise*. Accessed: 2025-01-24. Energy research Centre of the Netherlands. Rome, Italy, Apr. 2011. URL: https://publications.tno.nl/publication/34631409/25yV9X/m12004.pdf.

[16] Pat Moriarty. *NAFNoise: NREL AirFoil Noise*. https://www.nrel.gov/wind/nwtc/naf-noise.html. Accessed: 2025-01-24. 2005.

[17] Delf University of Technology, 2025. URL: https://www.tudelft.nl/lr/organisatie/afdelingen/flow-physics-and-technology/facilities/low-speed-wind-tunnels/a-tunnel.

[18] Alejandro Rubio Carpio et al. "Experimental characterization of the turbulent boundary layer over a porous trailing edge for noise abatement". In: *Journal of Sound and Vibration* 443 (2019), pp. 537–558. ISSN: 0022-460X. DOI: https://doi.org/10.1016/j.jsv.2018.12.010. URL: https://www.sciencedirect.com/science/article/pii/S0022460X18308277.

[19] Technical University of Denmark DTU, 2025. URL: https://www.plct.dk/.

[20] . *Blade Extensions for Silent Turbines, Final report (public)*. Tech. rep., June 2025.

[21] Guillem Verges i Plaza and Andreas Fischer and Oliver Lylloff and Christian Bak and Anders S. Olsen and Franck Bertagnolio and Salil Luesutthiviboon and Lourenco Tercio Lima Pereira and Daniele Ragni and Francesco Avallone and Alexandre Suryadi and Michaela Herr. *Benchmarking of the NACA 633-018 Trailing-Edge Noise in a Broad Reynolds Number Range as Part of the IEA Task 39*. Tech. rep. AIAA 2022-2981. AIAA, 2022.

[22] A.L. Braslow and E.C. Knox. *Simplified Method for Determination of Critical Height of Distributed Roughness Particles for Boundary-layer Transition at Mach Numbers from 0 to 5*. Tech. rep. NACA-TN-4363. NACA, Sept. 1958.

[23] S. Oerlemans, P. Sijtsma, and B. Méndez López. "Location and quantification of noise sources on a wind turbine". In: *Journal of Sound and Vibration* 299.4 (2007), pp. 869–883. ISSN: 0022-460X. DOI: https://doi.org/10.1016/j.jsv.2006.07.032. URL: https://www.sciencedirect.com/science/article/pii/S0022460X06006316.

[24] S. Luesutthiviboon. "Assessing and improving trailing-edge noise reduction technologies for industrial wind-turbine applications". Award date: 14 Oct 2022, Supervisors: M. Snellen, D. Ragni, Advisor: D.G. Simons. Dissertation (TU Delft). Delft University of Technology, 2022. URL: https://doi.org/10.4233/uuid:23e2f72e-2502-4f4a-9504-ba607bae0364.

[25] Philip J. Morris, Lyle N. Long, and Kenneth S. Brentner. "An Aeroacoustic Analysis of Wind Turbines". In: *42nd AIAA Aerospace Sciences Meeting and Exhibit*. Reno, Nevada: American Institute of Aeronautics and Astronautics, Jan. 2004. DOI: 10.2514/6.2004-1184.

[26] F. Bertagnolio, H. Aa. Madsen, and A. Fischer. "A combined aeroelastic-aeroacoustic model for wind turbine noise: verification and analysis of field measurements". In: *Wind Energy* 20.8 (2017), pp. 1331–1348. DOI: 10.1002/we.2096. URL: https://onlinelibrary.wiley.com/doi/full/10.1002/we.2096.

[27] Yannick D. Mayer et al. "A semi-analytical noise prediction model for airfoils with serrated trailing edges". In: *Renewable Energy* 143 (2019), pp. 679–691. ISSN: 0960-1481. DOI: https://doi.org/10.1016/j.renene.2019.04.132. URL: https://www.sciencedirect.com/science/article/pii/S0960148119306172.

[28] Benshuai Lyu and Lorna J. Ayton. "Rapid noise prediction models for serrated leading and trailing edges". In: *Journal of Sound and Vibration* 469 (2020), p. 115136. ISSN: 0022-460X. DOI: https://doi.org/10.1016/j.jsv.2019.115136. URL: https://www.sciencedirect.com/science/article/pii/S0022460X19306996.

[29] Guannan Wang et al. "Aero-acoustic prediction tool for complex wind turbine blade configurations". In: *Proceedings of the 10th International Conference on Wind Turbine Noise*. Accessed: 2025-01-27. LM Wind Power. Dublin, Ireland, June 2023. URL: https://www.researchgate.net/profile/Jeremy-Hurault/publication/371911183_Aeroacoustic_Prediction_Tool_for_Complex_Wind_Turbine_Blade_Configurations/links/649be0ccc41fb852dd39e57d/Aeroacoustic-Prediction-Tool-for-Complex-Wind-Turbine-Blade-Configurations.pdf.

[30] K. Boorsma et al. *Smart Rotor Design, Technology Assessment*. Tech. rep. ECN-X–11-154. ECN, Dec. 2011.

[31] J. Jonkman et al. *Definition of a 5-MW Reference Wind Turbine for Offshore System Development*. Tech. rep. NREL/TP-500-38060. NREL, Feb. 2009.

Energy & Materials Transition

Westerduinweg 3
1755 LE Petten
www.tno.nl

TNO innovation for life